

3DRot: 3D Rotation Augmentation for RGB-Based 3D Tasks

Shitian Yang^{1*}, Deyu Li^{1,2*}, Xiaoke Jiang^{1‡}, Lei Zhang¹

¹International Digital Economy Academy (IDEA)

²Shenzhen University

{syang214@jh.edu, 2300432059@email.szu.edu.cn, jiangxiaoke@idea.edu.cn, leizhang@idea.edu.cn}

Abstract

RGB-based 3D tasks, e.g., 3D detection, depth estimation, 3D keypoint estimation, still suffer from scarce, expensive annotations and a thin augmentation toolbox, since most image transforms, including resize and rotation, disrupt geometric consistency. In this paper, we introduce 3DRot, a plug-and-play augmentation that rotates and mirrors images about the camera’s optical center while synchronously updating RGB images, camera intrinsics, object poses, and 3D annotations to preserve projective geometry-achieving geometry-consistent rotations and reflections without relying on any scene depth. We validate 3DRot with a classical 3D task, monocular 3D detection. On SUN RGB-D dataset, 3DRot raises IoU_{3D} from 43.21 to 44.51, cuts rotation error (ROT) from 22.91° to 20.93°, and boosts $mAP_{0.5}$ from 35.70 to 38.11. As a comparison, Cube R-CNN adds 3 other datasets together with SUN RGB-D for monocular 3D estimation, with a similar mechanism and test dataset, increases IoU_{3D} from 36.2 to 37.8, boosts $mAP_{0.5}$ from 34.7 to 35.4. Because it operates purely through camera-space transforms, 3DRot is readily transferable to other 3D tasks.

Introduction

RGB-based 3D perception has become a cornerstone of robotics, autonomous driving, and augmented-reality workflows. However, curating large-scale 3D datasets is far more expensive and time-consuming than labeling 2D images: annotators must specify metric object poses and sizes, often with laser scans or multi-view capture, and reports show that 3D boxes can cost several-fold more per instance than 2D boxes. Data scarcity consequently bottlenecks generalization and fuels the search for synthetic diversity (Brazil et al. 2023). Focusing on non-generative, non-insertion, plug-and-play augmentations, today’s RGB-based 3D detection pipelines still rely on a narrow menu-chiefly random scaling and cropping (with intrinsic updates), horizontal flips (and only rarely vertical flips), and global color jitter-because any transform must preserve geometric consistency so that augmented objects remain physically plausible in the scene (Brazil and Liu 2019; Li et al. 2022; Zou et al. 2021; Chen et al. 2020; Li, Jia, and Shi 2024). Indeed,

naively pasting objects at arbitrary depths or orientations injects implausible scale-depth cues and can hurt detector accuracy (Ge et al. 2023; Li, Jia, and Shi 2024; Parihar et al. 2025).

Beyond the ubiquitous color jitters trick inherited from 2D detection pipelines, 3D perception currently relies on three fairly disjoint families of data-augmentation techniques:

(1) Geometry-Consistent Camera/Scene Transforms.

These methods perturb the camera pose or the ground plane and re-project all annotations, thereby preserving the exact 2D–3D correspondence. Typical operations include scaling, cropping, ground-plane-constrained rotations, and flipping (Lian et al. 2022; Engilberge et al. 2023). In multi-sensor fusion and multi-view settings, flipping is a common choice as long as the transformation is applied consistently across modalities/views (Wang et al. 2021; Pan et al. 2025). The advantages are simplicity, no rendering pipeline, and plug-and-play integration; however, the operation set remains narrow, and rotation augmentation is restricted to in-plane/coplanar assumptions and thus cannot be directly used when views or data are not approximately coplanar.

(2) Physically Plausible Instance/Object Insertion.

These approaches cut object instances from real scenes or CAD repositories, paste them in 3D or BEV, and synchronize the RGB projections while explicitly handling occlusion and scale (Wang et al. 2021; Ge et al. 2023; Parihar et al. 2025). The main drawback is the heavy overhead of scene reconstruction and photometric harmonization (e.g., collision checks, lighting/shadow consistency), which hampers scalability across domains.

(3) Synthetic / Generative and Weak-Supervision Pipelines.

These pipelines first reconstruct the 3D scene (or novel viewpoints), then edit objects or cameras in the 3D world and re-render to produce training images (Wang et al. 2024; Cheng et al. 2025; Chang et al. 2024). Geometric consistency is guaranteed by the rendering process and the resulting realism can be photo-realistic; nevertheless, reconstruction and rendering are computationally expensive, and iteration cycles are slow.

Recent progress has gravitated toward physically realistic instance insertion and generative/weakly supervised pipelines rather than toward truly plug-and-play primitives. Object insertion methods synthesize diversity by pasting CAD or real instances with explicit occlusion/scale handling

*This work was done during an internship at the International Digital Economy Academy (IDEA).

‡Corresponding author.

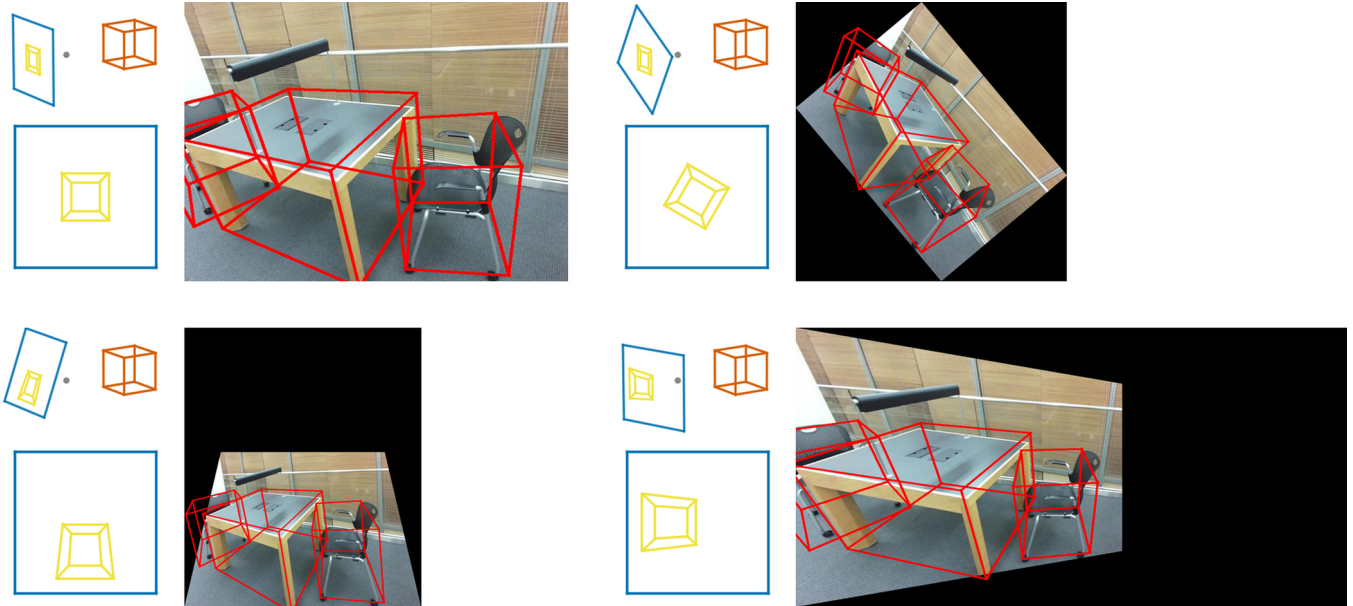


Figure 1: Overall concept of 3DRot. We rotate images about the camera’s optical center and synchronously update intrinsics, poses, and labels to preserve projective geometry. In each panel, the left subfigure is a concept sketch: red denotes the 3D bounding box, blue the screen border, and yellow the projected 3D box on the screen. Panels: top-left (origin), top-right (yaw 50°), bottom-left (roll 20°), bottom-right (pitch 20°).

(Ge et al. 2023; Parihar et al. 2025), while generative routes reconstruct scenes or viewpoints and then re-render (Wang et al. 2024; Cheng et al. 2025; Chang et al. 2024). Consequently, the most fundamental RGB-based setting, monocular RGB, still relies primarily on horizontal flips and mild color jitter (Brazil and Liu 2019; Li et al. 2022; Zou et al. 2021; Chen et al. 2020; Li, Jia, and Shi 2024), while in-plane rotation—an indispensable and highly effective augmentation in 2D recognition—remains largely untapped in 3D settings. However, naive rotation or pasting of objects in 3D space can destroy tight depth-scale coupling and violate geometric consistency, leading to a degraded detector accuracy (Ge et al. 2023; Li, Jia, and Shi 2024; Parihar et al. 2025). Even the ubiquitous horizontal flip still lacks a principled account of when and why it helps. These observations motivate us to devise a plug-and-play, geometry-aware augmentation module that enriches object-pose diversity without information loss, alleviates annotation scarcity, and lays the groundwork for more sophisticated, geometry-driven augmentations in future work.

In this paper, we propose Optical Center 3D Rotation Augmentation (3DRot), a plug-and-play module that enriches RGB-based 3D training data by rotating and mirroring scenes about the camera’s optical center while rigorously preserving projective geometry as shown in Fig. 1. For each desired in-plane rotation or reflection, 3DRot derives an exact homography from the camera projection matrix, enabling one-to-one pixel remapping without depth hallucination; the same closed-form transformation keeps the RGB image, 3D data, and camera intrinsics mutually consistent, delivering depth-free, geometry-faithful augmentation that

drops seamlessly into existing 3D tasks.

As a fundamental RGB-based 3D task, monocular 3D detection serves as our representative testbed to demonstrate the effectiveness of 3DRot. We validate 3DRot by inserting it into a frozen DINO-X (Ren et al. 2024; Liu et al. 2024) + Cube R-CNN head (Brazil et al. 2023) with matched schedules. On SUN RGB-D 10-category split (SUN10) (Song, Lichtenberg, and Xiao 2015), it improves IoU_{3D} from 43.21 to 44.51, lowers ROT from 22.91° to 20.93°, and increases $mAP_{0.5}$ from 35.70 to 38.11; smaller but consistent gains appear on SUN10. Ablations confirm geometry-consistent rotations and chirality-safe flips as the main drivers, with principal-point realignment providing a minor additional benefit.

Related Works

Compared with 2D vision benchmarks, 3D datasets are markedly smaller, offer fewer augmentation strategies, and therefore generalize less well. Yet real-world 3D perception must cope with dramatic viewpoint changes: robot wrist joints and pan-tilt heads constantly pitch and yaw; drones undergo rapid yaw and roll in flight, tilting the camera’s optical axis; dashcams, roadside infrastructure cameras, and vehicle-mounted sensors experience pitch/roll disturbances during braking or on inclines; and every hand-held AR/MR capture introduces random orientations with each lift or wrist twist. Robust, geometry-consistent augmentations are thus essential for closing the gap between limited training data and these demanding, off-axis scenarios.

RGB-based Rotation Augmentation

Early attempts to regularize RGB-based networks with viewpoint changes started from settings in which the depth channel is readily available, so the augmentation can be expressed directly in camera space. Keypoint-based Monocular 3D Object Detector (Kim et al. 2020) injects small perturbations into the robot-mounted camera’s roll, pitch and yaw and then re-project SUN RGB-D boxes to match the new pose. While this improves robustness to head motions, it still relies on full RGB-D frames. Two-level Data Augmentation (Engilberge et al. 2023) pushes consistency a step further: their two-level scheme first applies an in-plane homography to each calibrated view and then corrects the per-view projection matrix so that all images still meet at a common ground plane. The operation is, however, intrinsically *coplanar*; any 3D structure that rises above or falls below the reference plane (e.g. shelves or hanging objects) accumulates geometric error after transformation. Most recently, GroundMix (Meier et al. 2024) shows that simple in-plane rotations around the optical axis suffice for monocular car- and drone-view detectors; they adjust 3D yaw accordingly and keep the remaining pose angles fixed. This assumption holds only when the camera truly spins about its z -axis; moreover, it offers no rigorous proof of geometric consistency, merely demonstrating visual plausibility.

RGB-based Flipping Augmentation

Random horizontal flipping is the most widely used geometry-aware transform in RGB-based tasks because it is *label-preserving* for the image plane and inexpensive to implement. The pioneering (Brazil and Liu 2019) pipeline reflects each 3D box corner on the image, then back-projects the flipped vertices with the original depth to obtain an updated 3D cuboid, leaving all other pose parameters. Although effective for heading predictions, this strategy cannot propagate sign changes to the off-diagonal entries of a full 3×3 rotation matrix and therefore assumes that only the yaw angle is modeled. Several follow-up methods (Chen et al. 2020; Zou et al. 2021; Li et al. 2022; Li, Jia, and Shi 2024; Wang et al. 2021; Pan et al. 2025) inherit the same augmentation. Cube R-CNN (Brazil et al. 2023) introduces a more principled update: it composes two mirror matrices, one for the image warp and one for the camera coordinate frame, so that the predicted $R \in SO(3)$ remains valid after a flip. This design finally enables horizontal mirroring for full-angle pose regression, but the derivation presumes that the principal point coincides with the image center; when intrinsics are asymmetric or cropped, the 2D-3D alignment still drifts.

Other Augmentations

Beyond rotations and flips, several geometry-aware strategies have been explored to enrich RGB-based 3D data. Geometric Consistency Augmentation (Lian et al. 2022) introduces four camera-centric manipulations-random scaling, random cropping, camera translation, and instance-level copy-paste-each designed to preserve depth cues after image warping. While these augmentations improve robust-

ness, random cropping can discard large portions of background context, and the copy-paste pipeline requires dense depth maps plus heuristic rules to blend pasted objects seamlessly. 3D Copy-Paste (Ge et al. 2023) makes this idea more rigorous by sampling physically plausible insertions from an external CAD library: candidate objects are resized, posed, and lit to avoid collisions and match the scene illumination, yielding more realistic composites. Nevertheless, its rendering loop and collision search add notable pre-processing cost, and downstream accuracy still depends on perfect plane reconstruction and light estimation. Moreover, random cropping risks discarding the background context that conveys important geometric cues, while instance-level copy paste—despite its popularity—relies on intricate manual placement heuristics and still falls short of producing truly photorealistic composites (Li, Jia, and Shi 2024).

Method

3DRot applies an arbitrary camera-centric rotation (pitch, roll, yaw; optional mirroring) about the optical center and warps the image using the corresponding pure-rotation homography. This keeps updates to the camera frame and screen space consistent and preserves the projection geometry. We first outline the framework and notation, then derive the rotation model and label-synchronization rules. Intuitively, 3DRot rotates each pixel’s viewing ray about the optical center, preserving all geometric correspondences without introducing any new quantities that would need to be re-estimated.

To maintain the geometric projection relationship, two principal transformations must be rigorously defended. Firstly, the transformation defining the object’s pose relative to the camera must remain consistent with the applied rotation. Secondly, the projective transformation from the camera coordinate system to the image plane must be preserved.

Coordinate System & 3D BBOX Transformation

To propagate a virtual camera rotation to all scene geometry, we must first clarify how 3D points migrate between the world frame, the original camera frame, and the rotated camera frame. Accordingly, this subsection revisits the world-to-camera transform, derives the point-wise update induced by a camera-centric rotation, and then lifts the result to the cuboid pose that will be used throughout the remainder of the method.

A point expressed in the world frame is mapped to the camera frame through the following transform:

$$T_c = RT_w + t \quad (1)$$

where $T_c \in \mathbf{R}^{3 \times 1}$ represents a 3D point location in camera’s coordinate system, $T_w \in \mathbf{R}^{3 \times 1}$ represents a 3D point location in world’s coordinate system, $R \in \mathbf{R}^{3 \times 3}$ and $t \in \mathbf{R}^{3 \times 1}$ represent camera extrinsics. After rotating the camera, the new camera’s coordinate system should be:

$$T_{rot-c} = R_c T_c \quad (2)$$

Combined (1) and (2):

$$T_{rot-c} = R_c R T_w + R_c t \quad (3)$$

(3) indicates that the camera extrinsics should be updated if rotation augmentation is applied.

The previous derivation shows how any single 3-D point is transferred from the original camera frame to the rotated one. We now extend this result to an entire axis-aligned cuboid, whose pose is parameterized by its translation, sizes, and rotation matrix. Let

$$T_{bb} = R_{bb} S_{bb} + t_{bb} \quad (4)$$

denote the 3×8 matrix of the eight cuboid corners in the *original* camera coordinates, where the column matrix $S_{bb} \in \mathbf{R}^{3 \times 8}$ is formed by concatenating the vectorized offsets $(\pm \frac{W}{2}, \pm \frac{H}{2}, \pm \frac{L}{2})^\top$.

Applying the camera-centric rotation (2) to every corner gives

$$T_{bb}^{new} = R_c (R_{bb} S_{bb} + t_{bb}) = \underbrace{(R_c R_{bb})}_{R_{new}} S_{bb} + \underbrace{R_c t_{bb}}_{t_{new}},$$

hence the updated pose parameters are

$$R_{new} = R_c R_{bb}, \quad S_{new} = S_{bb}, \quad t_{new} = R_c t_{bb}.$$

That is, the cuboid's orientation and translation are left-multiplied by the camera rotation R_c , whereas its side lengths remain unchanged.

Projective Transformation

Having established how the 3D coordinates of each scene point are updated under a camera-centric rotation, we now turn to their image-plane projections. Specifically, we must determine how every pixel location transforms so that the rotated view remains geometrically consistent with the new camera frame. To this end, we (i) recap the pinhole-projection equation, (ii) derive the homography that arises when the camera rotates about its optical center, and (iii) show how this homography simplifies to a pure-rotation form that is valid for *any* 3D scene, without the usual planarity assumption or depth information. These steps yield a closed-form mapping $H = K' R_c K^{-1}$ which we will use to warp the RGB image, masks, and NOCS maps (Krishnan et al. 2024) in the remainder of the pipeline.

The projective transformation from the camera coordinate system to the image plane can be represented by the following.

$$P = \frac{1}{z} K T_c \quad (5)$$

where $P = [u, v, 1] \in \mathbf{R}^{3 \times 1}$ represents a pixel location in the image, z represents the depth of the 3D point in camera space, and K represents camera's intrinsics.

Equation (5) defines the projection for a single point. If we consider a scenario where the observed 3D points all reside on a single plane S , the relationship between A camera view and B camera view of this plane can be simplified. In such cases, any two images of the same planar surface in space are related by a homography:

$$P_A = \frac{z_B}{z_A} K_A H_{AB} K_B^{-1} P_B \quad (6)$$

where $P_A \in \mathbf{R}^{3 \times 1}$ belongs to image of camera A, $P_B \in \mathbf{R}^{3 \times 1}$ belongs to image of camera B. $H_{AB} \in \mathbf{R}^{3 \times 3}$ is defined by:

$$H_{AB} = R_{AB} - \frac{t_{AB} n^T}{d} \quad (7)$$

where $R_{AB} \in \mathbf{R}^{3 \times 3}$ is defined by $T_A = R_{AB} T_B$, $t_{AB} \in \mathbf{R}^{3 \times 1}$ is defined by $T_A = T_B + t_{AB}$. $d \in \mathbf{R}^1$ represents the distance from the optical center of camera B to plane S , $n^T \in \mathbf{R}^{3 \times 1}$ represents the normal vector of the single plane S and $n^T S + d = 0$. (Hartley and Zisserman 2004; Szeliski 2022)

The application of Eq. (7) for the homography H_{AB} presupposes that the observed 3D points lie on a common plane, denoted as S . This coplanarity constraint is embedded within the definition of H_{AB} .

However, in the specific context of rotational data augmentation, the camera undergoes rotation around its optical center without any translational movement. Consequently, the translation vector t_{AB} becomes zero ($t_{AB} = 0$). Substituting this into Eq. (7), the homography matrix simplifies to $H_{AB} = R_{AB}$.

Therefore, for data augmentation involving only rotation around the optical center, Eq. 6 can be reformulated as:

$$P_A = \frac{z_B}{z_A} K_A R_{AB} K_B^{-1} P_B \quad (8)$$

Crucially, this simplified Eq. (8) no longer requires the coplanarity of 3D points. As a result, Eq. (8) is applicable to any arbitrary 3D scene, provided that the camera transformation consists solely of rotation about its optical center. Hence we treat the transformation as a pure rotation about the optical center, omitting any translation term.

It is important to note that P_A and P_B , while elements of $\mathbf{R}^{3 \times 1}$, represent points on their respective image planes in homogeneous coordinates, typically of the form $[u, v, 1]^T$. Given that the third component of these homogeneous image coordinates is inherently 1 (after normalization), the scaling factor $\frac{z_B}{z_A}$ in Eq. (8) can be conceptualized as a normalization constant denoted by λ . This scalar λ ensures that the resulting vector P_A is correctly scaled to its homogeneous representation where the last component is 1. Thus, Eq. (8) can be expressed in a more general form, highlighting the projective transformation up to a scale factor:

$$P_A = \lambda K_A R_{AB} K_B^{-1} P_B \quad (9)$$

Here, λ encapsulates the necessary scaling (equivalent to $\frac{z_B}{z_A}$) to maintain the equality for the chosen homogeneous representation of P_A . This form underscores that the geometric core transformation that relates the image points under pure camera rotation is $K_A R_{AB} K_B^{-1}$, with λ accounting for the projective scaling.

By synthesizing Eq. (3), Eq. (5), and Eq. (9), we can articulate the comprehensive transformation from a world coordinate system to its projection on the image plane after camera rotation:

$$P_A = \lambda K_A (R_{AB} R_B T_w + R_{AB} t_B) \quad (10)$$

Flipping Transformation

Although analogous to rotation, flipping (reflection) augmentation is geometrically distinct. Rotations preserve chirality, while reflections invert it. Consequently, the geometric consistency of the reflection transformation must be validated for its use in our framework.

Accordingly, this subsection (i) formalizes a reflection with a matrix M , (ii) derives how M transforms 3D points and their image projections, and (iii) shows how to compose M with a preceding rotation so that the combined operator $R_c = M R$ can be applied in a single step. These results guarantee that flipping, alone or in combination with a rotation, preserves the geometric relationships required by our augmentation pipeline.

Let the projection in the original camera space be defined by Eq. (11):

$$z_A P_A = K_A T_A \quad (11)$$

After a reflection defined by a transformation matrix M , a 3D point T_A in the original camera space is mapped to a new point T_{AM} in the mirrored space:

$$T_{AM} = M T_A \quad (12)$$

The projection of this new point is subsequently governed by Eq. (13):

$$z_{AM} P_{AM} = K_{AM} T_{AM} \quad (13)$$

where K_{AM} represents the intrinsic parameters corresponding to the mirrored view.

By substituting the object pose from Eq. (1) and Eq. (11) into Eq. (12), we can determine the new pose in the mirrored camera system. The original pose (R_A, t_A) is transformed into $(M R_A, M t_A)$. Consequently, the comprehensive transformation from the world's coordinate system to the mirrored image plane is given by:

$$P_{AM} = \lambda K_{AM} (M R_A T_w + M t_A) \quad (14)$$

This demonstrates that reflection can be consistently integrated as a valid geometric transformation applied directly to the object's pose parameters.

Furthermore, this formulation allows reflection to be seamlessly composed with rotation. A composite transformation can be applied where the object's pose (R_A, t_A) is first rotated by R and subsequently reflected by M . The final pose becomes $(M R R_A, M R t_A)$, leading to the final projection equation:

$$P_{AM} = \lambda K_{AM} (M R R_A T_w + M R t_A) \quad (15)$$

$$P_{MR} = \lambda K_{MR} M R K_A^{-1} P_A \quad (16)$$

This confirms the geometric consistency of combining these augmentation techniques.

General Linear Transformation

The derivation in Eq. (12) does not hinge on M being a pure reflection; any invertible linear operator $A \in R^{3 \times 3}$ can replace M . The camera-to-image mapping remains a single matrix product $H_A = K_A A K_A^{-1}$, so 2D-3D points stay geometrically consistent under the new view.

Loss of cuboid structure. Unlike reflections or rotations, a general linear (or affine) transform distorts the unit axes unequally; therefore an axis-aligned 3D bounding box is mapped to a *parallelepiped* rather than a rectangular cuboid. To retain the canonical (R, t, s) representation after an affine transform $A \in GL(3)$, we require that the transformed cuboid again factorizes into an *orthogonal* rotation, a *diagonal* size matrix, and a translated center. Applying A to the eight corners of the original box yields with $R_A \in SO(3)$ and $D_A = \text{diag}(d_1, d_2, d_3)$ yet to be determined.

$$T_{bb}^{new} = A(R_{bb} S_{bb} + t_{bb}) = \underbrace{(R_A R_{bb})}_{R_{new}} \underbrace{(D_A S_{bb})}_{S_{new}} + \underbrace{A t_{bb}}_{t_{new}}$$

The required factorization can exist only if:

$$A R_{bb} = R_A R_{bb} D_A$$

We require an affine matrix $A \in R^{3 \times 3}$ such that, for *every* orthogonal matrix $O_1 \in O(3)$, there exist an orthogonal matrix O_2 and a diagonal matrix D satisfying

$$A O_1 = O_2 D.$$

Multiplying on the left by O_1^\top and on the right by its transpose gives

$$O_1^\top A^\top A O_1 = D^\top O_2^\top O_2 D = D^2.$$

Because the scene may contain objects under *arbitrary* orientations, the relation must hold for every rotation.

$$O_1^\top A^\top A O_1 = D^2, \quad \forall O_1 \in O(3)$$

Setting $O_1 = I$ yields $A^\top A = D^2$. Now recall the uniqueness theorem of second-order isotropic tensors (Reddy 2018): If a real symmetric tensor T satisfies $Q T Q^\top = T$ for all $Q \in O(3)$, then $T = \lambda I$.

Applying this to the symmetric tensor $T = A^\top A$ gives $A^\top A = \lambda^2 I$, hence $A = \lambda R_A$ for some $\lambda > 0$ and $R_A \in O(3)$. In the context of axis-aligned cuboids we further fix $R_A = I$, so the only admissible affine map is a uniform scaling $A = \lambda I$. Affine transforms with shears or non-uniform scalings therefore cannot preserve the (R, t, s) factorization for all poses and are left to the *Discussion* section for domain-specific treatment.

Image Padding and Principal-Point Realignment

Rotating an image about the pitch or roll axes warps its footprint on the image plane; the resulting view no longer fits the original rectangular support. A naive crop or resize would either discard valid pixels or break the projective consistency implied by the intrinsic matrix.

Screen coordinates place the origin at the top-left corner $(0, 0)$, whereas camera intrinsics locate the principal point (c_x, c_y) near the image center. After rotation, points that

were inside the frame can land at negative coordinates if projected with the original intrinsics. Translating the image to make all pixels positive and then cropping back to the original size therefore shifts the geometric center away from the declared principal point, corrupting downstream geometry.

We prevent this with a three-step procedure that both preserves every pixel and keeps the principal point at the center of the final canvas:

1. **Project the original corners.** Let P_{orig} be the four image corners and R the applied camera rotation. Define K_0 to equal the source intrinsics K_A but with principal point $(0, 0)$. The corners in the rotated frame are

$$P'_{\text{rot}} \propto K_0 R K_A^{-1} P_{\text{orig}}.$$

2. **Compute the bounding box.** After homogeneous normalization, write the image-space coordinates as (u'_j, v'_j) . The half-width and half-height of the minimal axis-aligned box centered on the optical axis are

$$x_{\max} = \max_j |u'_j|, \quad y_{\max} = \max_j |v'_j|.$$

3. **Update intrinsics and crop.** Build a new intrinsic matrix K_C equal to the source intrinsics K_A but with principal point (x_{\max}, y_{\max}) . Render the rotated image with K_C and finally crop the rectangle $[0, 2x_{\max}] \times [0, 2y_{\max}]$.

The $2x_{\max} \times 2y_{\max}$ canvas now contains every valid pixel from the rotation, while its center (x_{\max}, y_{\max}) exactly coincides with the principal point of K_C , preserving internal geometry.

Experiments

Datasets and Metrics

We build on OmniNOCS (Krishnan et al. 2024) and focus on its SUN RGB-D slice (Song, Lichtenberg, and Xiao 2015), retaining the ten furniture-centric categories *chair*, *table*, *desk*, *sofa*, *bed*, *nightstand*, *bookcase*, *dresser*, *toilet*, *bathtub*. To assess cross-domain generalization we curate additional 10-class split: an IN10 set that merges ARKitScenes (Baruch et al. 2021) and Hypersim (Roberts et al. 2021). Following Cube R-CNN, we discard objects with invalid depth or marginal image overlap and fix a handful of boxes whose third rotation-matrix column is not aligned with gravity.

We report seven metrics taken from Cube R-CNN and NOCSFormer (Brazil et al. 2023; Krishnan et al. 2024): IoU_{3D} , TRANS [cm], ROT [deg], SIZE [cm], 5GRAV, 10HEAD and $mAP_{0.5}$. IoU_{3D} is computed with the exact volumetric intersection between predicted and ground-truth cuboids, not the fast approximation used in the original Cube R-CNN code. AP denotes mean Average Precision at a fixed 2D IoU threshold of 0.5. $mAP_{0.5}$ averages AP over the nine 3D IoU thresholds $\{0.05, 0.10, \dots, 0.50\}$, providing a finer-grained view of performance. 5GRAV is the percentage of predictions with gravity-axis error $< 5^\circ$; 10HEAD is the percentage with heading (yaw) error $< 10^\circ$ (Krishnan et al. 2024). For IoU_{3D} , 5GRAV, 10HEAD and $mAP_{0.5}$ higher values indicate better performance, whereas lower values are preferred for TRANS, ROT, and SIZE.

Implementation Details

We adopt DINO-X (Ren et al. 2024; Liu et al. 2024), a DETR-style detector whose hybrid CNN-Transformer encoder produces highly accurate 2D boxes and class logits across diverse indoor datasets. Although the original model is pre-trained with open-vocabulary text supervision, we use it purely as an off-the-shelf 2D *object recognizer*: all backbone and detection layers are kept *frozen* during our experiments.

The last decoder layer produces $N=900$ object queries (256 dims). We feed the corresponding image features into a Cube R-CNN head (Brazil et al. 2023), which predicts a 9-D cuboid representation-2D center, depth, 3D dimensions, and a full 3×3 rotation matrix.

We train for 1 000 epochs using AdamW (lr = 2×10^{-4}), MultiStepLR ($\gamma = 0.9$ at every 100 epochs), and clip gradients to an L_2 norm of 35.

Main Results

Table 1 summarizes single-run performance (seed 42) on the two evaluation splits. The first two rows correspond to the SUN10 setting: a vanilla DINO-X + Cube R-CNN baseline (labeled *SUN10*) and the same backbone equipped with 3DRot. Unless stated otherwise, 3DRot is applied with probability 0.8 for an in-plane rotation ($\text{yaw} \pm 10^\circ$, $\text{pitch/roll} \pm 5^\circ$) and probability 0.5 for a chirality-preserving horizontal flip; flips may be composed with the rotation within the same image.

On SUN10, 3DRot improves every metric: IoU_{3D} rises by 1.30, translation and size errors fall by 3.5% and 3.7%, and rotation error decreases by 8.6%. The largest relative gain is on orientation accuracy: 10HEAD increases from 47.3% to 55.5%, which also raises $mAP_{0.5}$ from 35.7% to 38.1%. For the IN10 indoor split the same augmentation brings a smaller yet consistent benefit ($\text{IoU}_{3D} +0.20$, translation -0.22 cm), showing that 3DRot does not overfit to SUN10 statistics.

Table 3 offers an additional perspective. All methods are evaluated on the identical SUN RGB-D test split; minor differences in training-set preprocessing do not affect the comparability of the reported results. The two Cube R-CNN lines are taken from the original Cube R-CNN paper: one model is trained only on SUN RGB-D, the other on the larger OMNI3DIN aggregate (SUN RGB-D, ARKitScenes, Objectron and Hypersim). Our detector, trained solely on SUN RGB-D and augmented with 3DRot, gains 1.30 IoU_{3D} over its own SUN baseline, providing a performance increase similar to that achieved by Cube R-CNN when switching to OMNI3DIN, yet without any extra training images.

Ablation Study

Notation. Baseline denotes the vanilla DINO-X + Cube R-CNN pipeline without any geometric augmentation. 0.5 F applies a horizontal flip with probability 0.5. (kc) indicates keep chirality: the mirrored image plane is mapped back to a right-handed camera frame. 0.8 R_{10-5-5} and 0.8 R_{30-5-5} sample yaw, pitch and roll from the symmetric angle ranges

Method	$IoU_{3D} \uparrow$	TRANS (cm) \downarrow	ROT (deg) \downarrow	SIZE (cm) \downarrow	5GRAV \uparrow	10HEAD \uparrow	$mAP_{0.5} \uparrow$
SUN10	43.21	11.60	22.91	12.93	78.03	47.32	35.70
SUN10 + 3DRot	44.51	11.19	20.93	12.45	79.89	55.53	38.11
IN10	30.39	22.97	31.34	13.62	79.71	38.01	—
IN10 + 3DRot	30.59	22.75	31.23	13.57	81.20	37.80	—

Table 1: Single-run results on SUN10 and IN10. All models share the same frozen DINO-X + Cube R-CNN backbone and training schedule. 3DRot applies a camera-centric rotation (with probability 0.8; yaw $\pm 10^\circ$, pitch/roll $\pm 5^\circ$) plus a chirality-preserving horizontal flip with probability 0.5; rotation and flip are composable.

Method	$IoU_{3D} \uparrow$	TRANS (cm) \downarrow	ROT (deg) \downarrow	SIZE (cm) \downarrow	5GRAV \uparrow	10HEAD \uparrow	$mAP_{0.5} \uparrow$
BS (Baseline)	43.21	11.60	22.91	12.93	78.03	47.32	35.70
BS + 0.5 F	43.35	11.24	25.36	12.68	26.59	47.97	35.84
BS + 0.5 F(kc)	43.79	11.43	20.91	12.61	78.67	55.23	36.58
BS + 0.8 R ₁₀₋₅₋₅	44.43	11.10	21.16	12.79	78.94	54.17	38.29
BS + 0.8 R ₃₀₋₅₋₅	43.89	11.22	21.70	12.60	81.30	52.38	37.53
BS + 0.8 R ₁₀₋₅₋₅ + 0.5F(kc)	44.51	11.19	20.93	12.45	79.89	55.53	38.11

Table 2: Ablation study on SUN10: effect of each augmentation component. All runs use the same training recipe as Table 1.

Method	Train set	$IoU_{3D} \uparrow$
Cube R-CNN	SUN RGB-D	36.2
Cube R-CNN	OMNI3DIN	37.8
Ours	SUN RGB-D	43.21
Ours + 3DRot	SUN RGB-D	44.51

Table 3: Evaluated on the SUN RGB-D 10-category split, using a category set closely aligned with Cube R-CNN

Method	Center	Chir.	$IoU_{3D} \uparrow$	ROT \downarrow	$mAP_{0.5} \uparrow$
Baseline	—	—	43.70	22.22	—
3DRot (full)	✓	✓	44.58	20.78	38.06
w/o Center	✗	✓	44.43	20.81	38.06
w/o Chirality	✓	✗	44.40	23.57	37.49

Table 4: Ablation on SUN10. To avoid information loss caused by the model’s downsampling, objects whose height is less than 6.25% of the image height are removed. Center: image padding & principal-point realignment. If Center is disabled, we simply crop to the rotated image’s post-rotation width and height; Chir.: chirality preservation during flips.

(in degrees) and apply them with probability 0.8. Flip and rotation are composed whenever both Bernoulli trials succeed.

Individual operators (Table 2). Adding flips alone (BS + 0.5 F) slightly raises IoU_{3D} but increases rotation error to 25.36° and collapses gravity alignment, indicating that a plain reflection is harmful. Activating keep-chirality (BS + 0.5 F(kc)) restores a low rotation error (20.91°) and yields a 10HEAD gain of 7.9. Pure rotation improves most metrics; the narrow band R₁₀₋₅₋₅ attains the highest AP, whereas the wider yaw range R₃₀₋₅₋₅ excels on 5GRAV. The full recipe-R₁₀₋₅₋₅ combined with chirality-safe flipping-achieves the best overall balance: lowest size error (12.45 cm), highest 10HEAD (55.53) and competitive detection scores ($mAP_{0.5} = 38.11$).

Center vs. Chirality (Table 4). Padding the rotated image and realigning the principal point (column Center) brings a small but consistent gain: removing it degrades IoU_{3D} from 44.58 to 44.43 and leaves $mAP_{0.5}$ unchanged. Chirality preservation is critical: turning it off inflates the rotation error from 20.78° to 23.57° and lowers $mAP_{0.5}$ by 0.57, confirming that naively mirroring a full 3×3 rotation matrix breaks orientation consistency.

Conclusion & Discussion

We have introduced 3DRot, a simple yet effective rotation-and-reflection augmentation that operates directly at the camera optical center. 3DRot does not require depth information for scene reconstruction while maintaining 2D-3D geometric consistency. Extensive experiments on SUN10 and IN10 show that 3DRot improves IoU_{3D} , rotation, gravity alignment and $mAP_{0.5}$ without any change to network architecture or loss weights. The gains generalize across domains and, on SUN RGB-D, rival those obtained by training on a dataset an order of magnitude larger.

Because 3DRot operates purely on camera extrinsics and a closed-form homography, it is readily transferable to other 3D vision tasks whose labels can be rotated in tandem, such as category-level NOCS alignment, human/robot keypoint estimation, or dense depth completion. Similarly, LiDAR-centric detectors could benefit from a hybrid variant that rotates point clouds and images jointly (Wang et al. 2021; Zhang, Wang, and Loy 2020).

Most indoor and outdoor benchmarks are gravity-aligned and near-vertical. The cameras’ roll angles during capture are tightly concentrated around zero. Rotation-centric augmentation is therefore especially valuable for domains with extreme or rapidly changing camera poses-e.g. wrist-mounted industrial manipulators or aerial drones-where robustness to arbitrary pitch, roll and yaw is critical.

All geometry-consistent augmentations-including 3DRot-can also serve as annotation auditors. Training two otherwise identical models, one with and one without such

an augmentation, and then comparing their results: a well-annotated dataset yields similar or higher performance by using geometry-consistent augmentations.

References

Baruch, G.; Chen, Z.; Dehghan, A.; Dimry, T.; Feigin, Y.; Fu, P.; Gebauer, T.; Joffe, B.; Kurz, D.; Schwartz, A.; et al. 2021. Arkitscenes: A diverse real-world dataset for 3d indoor scene understanding using mobile rgb-d data. *arXiv preprint arXiv:2111.08897*.

Brazil, G.; Kumar, A.; Straub, J.; Ravi, N.; Johnson, J.; and Gkioxari, G. 2023. Omni3d: A large benchmark and model for 3d object detection in the wild. In *Proceedings of the IEEE/CVF conference on computer vision and pattern recognition*, 13154–13164.

Brazil, G.; and Liu, X. 2019. M3d-rpn: Monocular 3d region proposal network for object detection. In *Proceedings of the IEEE/CVF international conference on computer vision*, 9287–9296.

Chang, M.; Lee, S.; Kim, J.; and Kim, N. 2024. Just Add \$100 More: Augmenting Pseudo-LiDAR Point Cloud for Resolving Class-imbalance Problem. *Advances in Neural Information Processing Systems*, 37: 66226–66259.

Chen, Y.; Tai, L.; Sun, K.; and Li, M. 2020. Monopair: Monocular 3d object detection using pairwise spatial relationships. In *Proceedings of the IEEE/CVF conference on computer vision and pattern recognition*, 12093–12102.

Cheng, H.; Xu, J.; Peng, L.; Yang, Z.; He, X.; and Wu, B. 2025. Object-level Data Augmentation for Visual 3D Object Detection in Autonomous Driving. In *ICASSP 2025-2025 IEEE International Conference on Acoustics, Speech and Signal Processing (ICASSP)*, 1–5. IEEE.

Engilberge, M.; Shi, H.; Wang, Z.; and Fua, P. 2023. Two-Level Data Augmentation for Calibrated Multi-View Detection. In *Proceedings of the IEEE/CVF Winter Conference on Applications of Computer Vision (WACV 2023)*, 128–136.

Ge, Y.; Yu, H.-X.; Zhao, C.; Guo, Y.; Huang, X.; Ren, L.; Itti, L.; and Wu, J. 2023. 3d copy-paste: Physically plausible object insertion for monocular 3d detection. *Advances in Neural Information Processing Systems*, 36: 17057–17071.

Hartley, R.; and Zisserman, A. 2004. *Multiple View Geometry in Computer Vision*. Cambridge, UK: Cambridge University Press, 2nd edition.

Kim, J.; Lee, G.; Kim, J.; Kim, H. J.; and Kim, K. 2020. Monocular 3D Object Detection for an Indoor Robot Environment. In *Proceedings of the 29th IEEE International Conference on Robot and Human Interactive Communication (IEEE RO-MAN 2020)*, 438–445.

Krishnan, A.; Kundu, A.; Maninis, K.-K.; Hays, J.; and Brown, M. 2024. OmniNOCS: A unified NOCS dataset and model for 3D lifting of 2D objects. In *European Conference on Computer Vision*, 127–145. Springer.

Li, Z.; Jia, J.; and Shi, Y. 2024. MonoLSS: Learnable sample selection for monocular 3D detection. In *2024 International Conference on 3D Vision (3DV)*, 1125–1135. IEEE.

Li, Z.; Qu, Z.; Zhou, Y.; Liu, J.; Wang, H.; and Jiang, L. 2022. Diversity matters: Fully exploiting depth clues for reliable monocular 3d object detection. In *Proceedings of the IEEE/CVF Conference on Computer Vision and Pattern Recognition*, 2791–2800.

Lian, Q.; Ye, B.; Xu, R.; Yao, W.; and Zhang, T. 2022. Exploring Geometric Consistency for Monocular 3D Object Detection. In *Proceedings of the IEEE/CVF Conference on Computer Vision and Pattern Recognition (CVPR 2022)*, 1685–1694.

Liu, S.; Zeng, Z.; Ren, T.; Li, F.; Zhang, H.; Yang, J.; Jiang, Q.; Li, C.; Yang, J.; Su, H.; et al. 2024. Grounding dino: Marrying dino with grounded pre-training for open-set object detection. In *European Conference on Computer Vision*, 38–55. Springer.

Meier, J.; Scalerandi, L.; Dhaouadi, O.; Kaiser, J.; Araslanov, N.; and Cremers, D. 2024. CARLA Drone: Monocular 3D Object Detection from a Different Perspective. In *Proceedings of the DAGM German Conference on Pattern Recognition (GCPR 2024)*, 137–152.

Pan, Y.; Cui, Q.; Yang, X.; and Zhao, N. 2025. How Do Images Align and Complement LiDAR? Towards a Harmonized Multi-modal 3D Panoptic Segmentation. In *Proceedings of the Forty-Second International Conference on Machine Learning (ICML)*. Vancouver, Canada: PMLR. Poster.

Parihar, R.; Sarkar, S.; Vora, S.; Kundu, J. N.; and Babu, R. V. 2025. MonoPlace3D: Learning 3D-Aware Object Placement for 3D Monocular Detection. In *Proceedings of the Computer Vision and Pattern Recognition Conference*, 6531–6541.

Reddy, J. N. 2018. Vectors and Tensors. In *An Introduction to Continuum Mechanics*, chapter 2, 57–58. Cambridge: Cambridge University Press, second edition.

Ren, T.; Chen, Y.; Jiang, Q.; Zeng, Z.; Xiong, Y.; Liu, W.; Ma, Z.; Shen, J.; Gao, Y.; Jiang, X.; et al. 2024. Dino-x: A unified vision model for open-world object detection and understanding. *arXiv preprint arXiv:2411.14347*.

Roberts, M.; Ramapuram, J.; Ranjan, A.; Kumar, A.; Bautista, M. A.; Paczan, N.; Webb, R.; and Susskind, J. M. 2021. Hypersim: A photorealistic synthetic dataset for holistic indoor scene understanding. In *Proceedings of the IEEE/CVF international conference on computer vision*, 10912–10922.

Song, S.; Lichtenberg, S. P.; and Xiao, J. 2015. SUN RGB-D: A RGB-D Scene Understanding Benchmark Suite. In *Proceedings of the IEEE Conference on Computer Vision and Pattern Recognition (CVPR)*, 567–576.

Szeliski, R. 2022. *Computer Vision: Algorithms and Applications*. Cham, Switzerland: Springer, 2nd edition.

Wang, C.; Ma, C.; Zhu, M.; and Yang, X. 2021. Pointaugmenting: Cross-modal augmentation for 3d object detection. In *Proceedings of the IEEE/CVF conference on computer vision and pattern recognition*, 11794–11803.

Wang, P.; Fan, Z.; Wang, Z.; Su, H.; Ramamoorthi, R.; et al. 2024. Lift3d: Zero-shot lifting of any 2d vision model to 3d. In *Proceedings of the IEEE/CVF Conference on Computer Vision and Pattern Recognition*, 21367–21377.

Zhang, W.; Wang, Z.; and Loy, C. C. 2020. Exploring data augmentation for multi-modality 3d object detection. *arXiv preprint arXiv:2012.12741*.

Zou, Z.; Ye, X.; Du, L.; Cheng, X.; Tan, X.; Zhang, L.; Feng, J.; Xue, X.; and Ding, E. 2021. The devil is in the task: Exploiting reciprocal appearance-localization features for monocular 3d object detection. In *Proceedings of the IEEE/CVF International Conference on Computer Vision*, 2713–2722.